Materials and Structures (2021)54:219
https://doi.org/10.1617/s11527-021-01819-2

ORIGINAL ARTICLE

Assessment of the post-fire residual bearing capacity of FRC and hybrid RC-FRC tunnel sections considering thermal spalling

Ramoel Serafini · Albert de La Fuente · Antonio D. de Figueiredo

Received: 10 March 2021 / Accepted: 4 November 2021

Abstract A design-oriented numerical model for the analysis of RC, FRC, and RC-FRC tunnel sections exposed to fire with different spalling parameters is presented. The numerical model is conceived in two steps: the first is the determination of the temperature field in the cross-section exposed to fire according to the spalling parameters; and the second is the determination of the bearing capacity of sections based on the thermal field in the section. At last, a parametric study was conducted to evaluate the effect of the fire curve, the spalling parameters, the reinforcement type, and the rebar's concrete cover on the bearing capacity of the sections. The results showed that the use of FRC as total or partial substitution to RC mitigates the fire-related reduction in the bearing capacity of the sections. Moreover, increasing the RC concrete cover is beneficial only if thermal spalling is avoided. When thermal spalling occurs, the FRC and RC-FRC solutions yielded the lowest reductions in the bearing capacity among the reinforcement solutions tested.

Keywords Fire · Fiber reinforced concrete · Thermal spalling · Bearing capacity · Tunnel lining

R. Serafini (✉) · A. D. de Figueiredo
Department of Civil Construction Engineering, Polytechnic Shool of the University of São Paulo, Avenida Professor Almeida Prado, Travessa 2, 83, São Paulo 05424-970, Brazil
e-mail: ramo.serafini@gmail.com

R. Serafini
Institute for Technological Research, Avenida Professor Almeida Prado 532, São Paulo 05508-901, Brazil

A. de La Fuente
Department of Civil and Environmental Engineering, Polytechnic University of Catalonia, Jordi Girona, 1-3, 08034 Barcelona, Spain

Published online: 14 November 2021

1 Introduction

Fiber reinforced concrete (FRC) is a composite material that may partially or totally replace the reinforced concrete (RC) in structural applications. In the last decades, a steadily increase trend in the amount of urban tunnels built with FRC pre-cast segments was verified due to the benefits provided by adding randomly distributed fibers into concrete [1]. When comparing the structural behavior of RC and FRC segments, the results of a full-scale experimental campaign show that the same load level conditions may be reached by FRC segments with advantages in terms of performance and cost [2]. The performance benefits are mostly related to the enhanced material's response to impact, diffused, and concentrated loads during the storage, transportation, and assembly of the pre-cast segments, as well as improved corrosion resistance [3–5].

In the last three decades, pernicious effects of fire were reported in several tunnels in Europe [6].

Table 1 Input parameters adopted for the thermo-mechanical simulation

Property	Input value
H (mm)	400
B (mm)	1000
f_{cd} (MPa)	45
f_{R3d} (MPa)	3.0
f_{sd} (MPa)	434
Initial temperature (°C)	25
Concrete density (kg/m^3)	2400
Specific heat (J kg^{-1} K^{-1})	900
Convective heat coefficient (W m^{-2} K^{-1})	25
Thermal conductivity (W m^{-1} K^{-1})	1.6
Emissivity	0.9

Because of this, researchers focused on evaluating the mechanical properties of FRC as a function of temperature [7–14] and developed progenitive full-scale experimental programs to evaluate the reductions in load bearing capacity and the deformation of the tunnel rings during fire [15]. In 2018, Di Carlo et al. [16] proposed a numerical model capable of assessing the bearing capacity of FRC sections considering different geometries, materials' properties, and fire scenarios. The numerical model employed a staggered analysis in which the thermal model computes the temperature distribution along the cross-section and the mechanical model computes the moment-axial (M–N) interaction envelopes based on the equilibrium equations. The aforementioned model was later implemented by other researchers in literature for the parametric analysis of a FRC subway line tunnel in the city of São Paulo, Brazil [17].

Moreover, advances have been reported in understanding the complex mechanisms governing the occurrence of thermal spalling in concrete, especially related to the influence of the materials' properties, the section geometry, and the fire scenario [18]. This phenomenon negatively affects the bearing capacity of tunnels [19] mostly due to the reduction of cross-sectional area, which may reach more than 50% in severe cases [15, 20]. In this sense, some predictive numerical models capable of estimating the occurrence of thermal spalling in plain concrete and FRC have been developed at micro- and meso-scale [21–24], however engineer-oriented models focused on the design of tunnels are scarce. More than that, the effect of spalling on the temperature distribution in the cross-section is often disregarded and this might lead to unsafe designs.

The current guidelines provide limited amount of information regarding the influence of fire and thermal spalling on the bearing capacity of FRC sections, as in state-of-the-art reports published by the ITA [25] and the *fib* Bulletin 46 [26]. The importance of evaluating the effect of spalling on tunnels is highlighted in the *fib* Bulletin 83, however the state-of-the-art report does not provide any spalling-related parameter to evaluate the fire resistance of tunnels [27]. Moreover, the *fib* MC-10 does not provide parameters oriented to the fire-design of FRC structures with or without the occurrence of thermal spalling [28]. Therefore, it is noticeable the lack of studies and parameters related to the effect of thermal spalling on the bearing capacity of tunnel segments. As a consequence, there are limited design-oriented tools to assess the fire safety conditions of TBM tunnels.

In this sense, the current paper presents a thermal–mechanical model to calculate the bearing capacity of RC, FRC, and hybrid RC-FRC sections exposed to fire considering the occurrence of thermal spalling. The bending bearing capacity is assessed by means of the bending-axial force (M–N) interaction envelopes, which are computed considering the distribution of temperatures and the respective mechanical properties in the cross-section. Finally, a parametric study varying the fire curve, the spalling parameters, the reinforcement type, and the concrete cover was conducted. Therefore, the results represent a valuable reference for standards and guidelines, as well as for designer's focused on tunnel structures.

2 Thermo-mechanical numerical model

This section presents the fundamental concepts for the development of the thermo-mechanical numerical model to assess the bearing capacity of the sections exposed to fire. The heat transfer model was based on the Fourier heat transfer equation [16, 17] and applied to the tunnel segments, while the mechanical model was based on the work of Di Carlo et al. [16]. The numerical model implemented for this study is based on a staggered analysis that decouples both thermal and mechanical problems, the thermal spalling

phenomenon being simulated by imposing spalling (R_{sp}) and section lost (s_L) rates. Even though the model developed simplifies the strongly dependent thermo-hygro-mechanical phenomena, it is valid and suitable for pre-design purposes.

2.1 Heat transfer model

The heat transfer through an isotropic solid body can be described by the Fourier heat transfer equation, as:

$$\nabla(KT) + Q = \rho C \tag{1}$$

where K is the thermal conductivity; c is the specific heat; p is the density; Q is the volumetric heat flux; T is the temperature; and t is the time. The heat transfer though concrete may be described in one-dimension planar conduction with no internal heat generated when considering a concrete fully hardened. This assumption may be considered in the central zone of the segments, which represents the greatest portion of the element. However, the regions of contact between segments may be better described by a two-dimension conduction since lateral heating may influence the temperature distribution [29], which needs to be addressed in future research. Based on this assumption and the discussion provided, Eq. 1 reduces to:

$$\alpha\left(\frac{\partial^2 T}{\partial z^2}\right) = \frac{\partial T}{\partial t} \tag{2}$$

where $\alpha = \frac{K}{\rho c}$.

In this sense, a numerical model based on the finite difference method (FDM) was developed to solve the Fourier heat transfer equation. The space–time domain was divided in preset constant values (discreate approach) and the differential equations were approximated by FDM. The numerical model adopted a closed space–time domain $\Re$:

$$\Re = \left\{(z,t) : 0 \le z \le L, 0 \le t \le t_{fire}\right\} \tag{3}$$

where z is the spatial variable; L is the length of the cross-section; t is the time related variable; and t_{fire} is the maximum duration of the fire event. The points within the space–time domain are equidistant and identified according to:

$$z_i = (i-1)\Delta z, \quad i = 1, 2, \ldots, n \tag{4}$$

$$t_j = (j-1)\Delta t, \quad j = 1, 2, \ldots, m \tag{5}$$

where n and m are the number of points and time instants, being $\Delta z = L/(n-1)$ and $\Delta t = t_{fire}/(m-1)$.

The computation of the second derivatives of the temperature with respect to the spatial variable at a point $z \in \Re$ were solved by the FDM approach, as:

$$\frac{\partial^2 T}{\partial z^2} = \frac{T(z+\Delta z, t) - 2T(z,t) + T(z-\Delta z, t)}{(\Delta z)^2} \tag{6}$$

while the first derivative of temperature related to time is computed as:

$$\frac{\partial T}{\partial t} = \frac{T(z, t+\Delta t) - T(z,t)}{\Delta t} \tag{7}$$

Substituting the Eqs. (6) and (7) into Eq. (2) it is possible to determine an equation to compute the temperature at $t = j+1$ given that the temperature at the $t = j$ is known, which is described as:

$$T_{i,j+1} = \left(1 - 2\overline{k}\right)T_{i,j} + \overline{k}\left(T_{i+1,j} + T_{i-1,j}\right) \tag{8}$$

where $\overline{k} = \alpha\Delta t/\Delta z^2$. The FDM results are stable if the condition $2\alpha\Delta t < \Delta z^2$ is satisfied. Considering that K is a function of temperature, a change in temperature scale is convenient to solve the thermal problem (see Di Carlo et al. [16]). Nevertheless, the numerical results obtained considering the independence of K from T were found to be sufficiently accurate from the design point of view when these were compared with the profiles presented in Di Carlo et al. [16].

2.2 Initial and boundary conditions

The room temperature thermal equilibrium is considered at the beginning of the numerical simulation. The net heat flux ($\dot{h}_{net}$) transferred from the fire source to the surface of the FRC segment is the sum of the heat flux components convection ($\dot{h}_c$) and radiation ($\dot{h}_r$), according to the Eq. (9):

$$\begin{aligned}\dot{h}_{net} &= \dot{h}_c + \dot{h}_r \\ &= \alpha_c\left(T_f - T_s\right) + \sigma\varepsilon\left[\left(T_f + 273\right)^4 - \left(T_s + 273\right)^4\right]\end{aligned} \tag{9}$$

where α_c is the convective heat transfer coefficient (in W m^{-2} K^{-1}); σ is the Stefan-Boltzmann constant (in W m^{-2} K^{-4}); ε is the dimensionless emissivity ranging from 0 (perfect reflector) to 1 (perfect absorber); T_f is the temperature of the fire source at

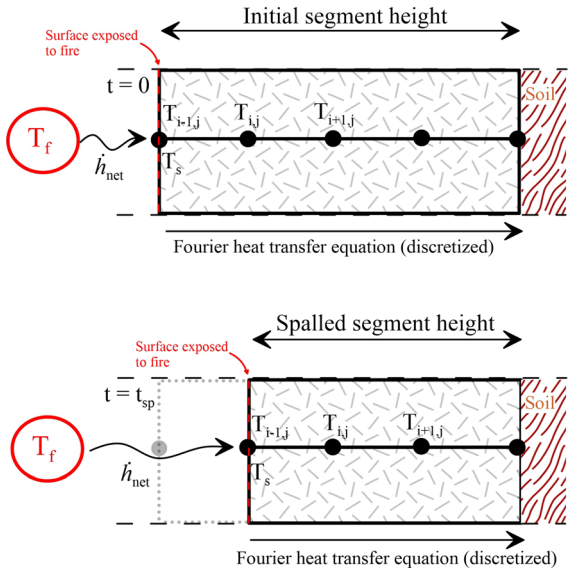

Fig. 1 Illustration of the heat transfer model developed

a given t value; and T_s is the temperature at the surface of the FRC segment at given t value. Figure 1 illustrates the heat transfer model developed considering the heat flux transferred and the convection described by the discretized Fourier heat transfer equation.

The effect of spalling is considered in the bearing capacity of FRC segments by reducing the height of the section (H) during the fire event accordingly. This reduction is implemented during the thermal simulation of the composite and results in a cross-section that varies as a function of time. The spalling rate (in mm/h) and the maximum depth of spalling (in mm) are considered the input parameter for simulating the spalling process. These parameters may be determined based on an experimental program using vertical fire simulators and a concrete mix representative of the segment [30]. In these experimental programs, spalling initiation time versus depth diagrams are often used to determine the spalling rate [31]. The spalling rate is established to compute the time required for a concrete thickness (Δz) exposed to elevated temperature to be spalled, by applying the Eq. (10).

$$t_{sp} = \frac{3600.\Delta z}{R_{sp}} \tag{10}$$

where t_{sp} is the time required for one discretized unit of Δz to be spalled (in seconds); R_{sp} is the experimentally determined rate of spalling (in mm/h); and Δz is the spatial subdivision of the section (same employed in Eq. 4). Therefore, the concrete thickness measuring Δz are removed from the thermal analysis every t_{sp} seconds until the maximum depth of spalling is reached.

Therefore, every t_{sp} seconds the spalling condition is reached, which results in the removal of the currently active Δz layer that is closer to the fire source. The removal of the Δz layer occurs by moving the position of the surface affected by fire (*i.e.* $T_{i-1,j}$) one discretized Δz unit toward the interior of the FRC and the spalled layer is disregarded in the heat transfer model implemented. In summary, the model takes into account that the heat transferred by the fire source, in the form of $\dot{h_c}$ and $\dot{h_r}$, begins to affect an inner region of the specimen (see Fig. 1), without considering the spalled layers. The aforementioned process occurs until the maximum depth of spalling accepted by the designer is reached. The considerations regarding the changes in the mechanical model as spalling occurs are provided in Sect. 3.2.

2.3 Thermal and physical properties of FRC

The thermal conductivity (K), specific heat (c), and density (ρ) of the FRC are time-dependent properties. In this sense, the changes in K, c, and ρ are assumed to vary similarly to plain concrete by the equations provided by the Eurocode [32]. The specific heat of concretes produced with siliceous and calcareous aggregates vary with temperature according to the Eq. (11).

$$c(T) = \begin{cases} 900, & 20\,^{\circ}\text{C} \le T \le 100\,^{\circ}\text{C} \\ 900 + (T - 100), & 100\,^{\circ}\text{C} < T \le 200\,^{\circ}\text{C} \\ 1000 + (T - 200), & 200\,^{\circ}\text{C} < T \le 400\,^{\circ}\text{C} \\ 1100, & 400\,^{\circ}\text{C} < T \le 1200\,^{\circ}\text{C} \end{cases} \tag{11}$$

where c is the specific heat of concrete (in J.kg^{-1} K^{-1}); and T is the temperature (in °C). The changes in density of concrete occurs due to the dehydration of hydrated products and consequent water loss, which may be computed by a multilinear equation as:

$$\rho(T) = \begin{cases} \rho_R, & 20\,^{\circ}\mathrm{C} \le T \le 115\,^{\circ}\mathrm{C} \\ \rho_R\left[1 - \dfrac{0.02(T-115)}{85}\right], & 115\,^{\circ}\mathrm{C} < T \le 200\,^{\circ}\mathrm{C} \\ \rho_R\left[0.98 - \dfrac{0.03(T-200)}{200}\right], & 200\,^{\circ}\mathrm{C} < T \le 400\,^{\circ}\mathrm{C} \\ \rho_R\left[0.95 - \dfrac{0.03(T-400)}{800}\right], & 400\,^{\circ}\mathrm{C} < T \le 1200\,^{\circ}\mathrm{C} \end{cases} \quad (12)$$

where ρ is the density of concrete as a function of temperature (in kg m^{-3}); ρ_R is the density of concrete at room temperature (in kg m^{-3}); and T is the temperature (in °C). The concrete density at room temperature was considered to be 2430 kg/m^3, based on the work of Serafini et al. [30]. Lastly, the thermal conductivity of normal-weight concretes exposed to temperatures between 20 and 1200 °C can be determined by the average of lower and upper limit values given by:

$$K_U = 2 - 0.2451\left(\frac{T}{100}\right) + 0.0107\left(\frac{T}{100}\right)^2 \quad (13)$$

$$K_L = 1.36 - 0.136\left(\frac{T}{100}\right) + 0.0057\left(\frac{T}{100}\right)^2 \quad (14)$$

where K_U is the upper limit for the thermal conductivity (in W m^{-1} K^{-1}); K_L is the lower limit for the thermal conductivity (in W m^{-1} K^{-1}); and T is the temperature (in °C).

3 FRC bearing capacity

3.1 Constitutive law

The constitutive law employed is based on a stress-block approach defined by the design compressive strength (f_{cd}) and the design post-crack tensile strength for the ultimate crack-opening (f_{Ftud}), as show in Fig. 2. The mechanical properties of the composite are influenced by the increase in temperature, which is computed by the use of coefficients of mechanical degradation as reduction factors in literature [12] and in design guidelines [32, 33].

In this context, the FRC compressive strength was calculated as a function of temperature based on the cylinder compressive strength and the respective coefficient of mechanical degradation, as:

$$f_{cd,T} = K_c \frac{f_{ck,R}}{\gamma_c} \quad (15)$$

where $f_{cd,T}$ is the design compressive strength at a given temperature (in MPa); K_c is temperature-dependent coefficient of mechanical degradation; $f_{ck,R}$ is the characteristic compressive strength at room temperature (in MPa); and γ_c is the partial safety factor, which is taken as $\gamma_c = 1$ in case of fire events [28]. The mechanical degradation of f_{cd} and f_{sy} are represented by K_c and K_{sy}, respectively, and defined as a function of temperature according to the values prescribed by the Eurocode [32], as shown in Fig. 3. The K_{sy} value is based on the reductions in the yield strength of hot rolled steel.

The behavior in tension is computed based on the rigid-plastic model presented by the *fib* Model Code 2010 [28] and the tensile strength for ultimate limit state (ULS) condition may be determined by the EN 14,651 three-point bending test procedure [34]. The design post-crack tensile strength of the composite can be calculated as a function of temperature, as:

$$f_{Ftud,T} = K_{Ftu} \cdot \frac{f_{R3k}}{3} \cdot \frac{1}{\gamma_F} \quad (16)$$

where $f_{Ftud,T}$ is the design post-crack tensile strength associated with the ultimate crack-opening (in MPa); K_{Ftu} is the coefficient of mechanical degradation for

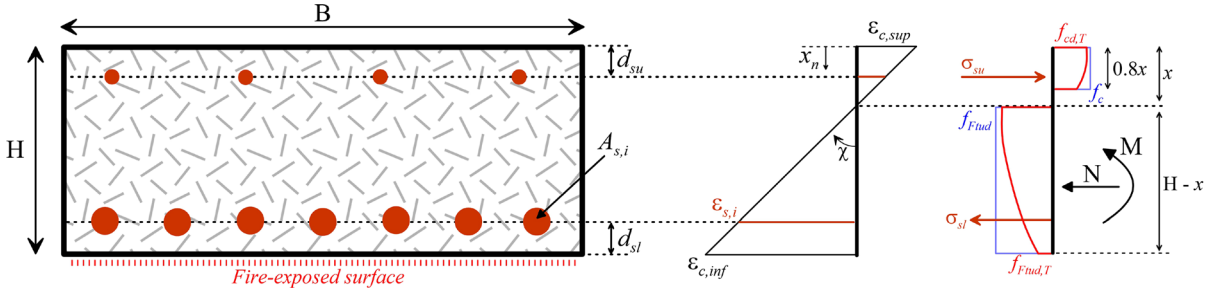

Fig. 2 Stress-block constitutive law adopted for the FRC

the post-crack tensile strength as a function of temperature; and f_{R3k} is the characteristic flexural tensile strength relative to the ULS at room temperature (in MPa). The mechanical degradation of f_{Ftud} is represented by K_{Ftu}, which is defined as a function of temperature according to the experimental results obtained by Serafini et al. [12] and presented in Fig. 3.

In cases where reinforcing steel is considered, the design yield strength of steel (f_{sd}) is reduced according to the yield strength reduction factor (K_{sy}) prescribed by the Eurocode [32], as described in Eq. (17).

$$f_{sd,T} = K_{sy}.f_{sy}.\frac{1}{\gamma_F} \tag{17}$$

where $f_{sd,T}$ is the design yield strength of steel (in MPa); K_{sy} is the coefficient of mechanical degradation for the yield strength of steel as a function of temperature; and f_{syk} is the characteristic steel yield strength at room temperature (in MPa).

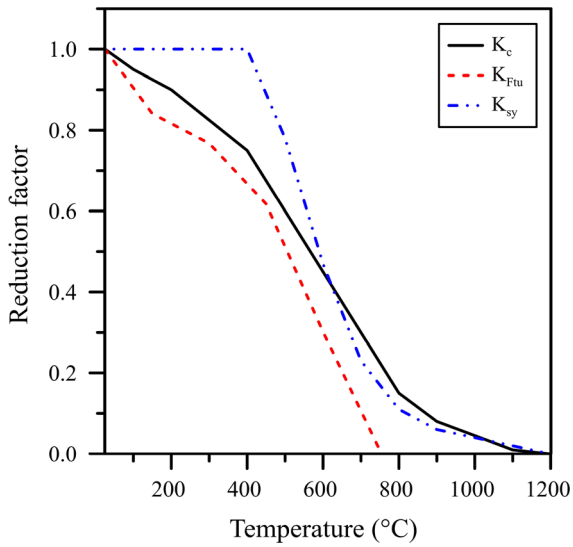

Fig. 3 Temperature-dependent coefficient of mechanical degradation for f_c and f_{Ftu}

3.2 Cross-sectional modelling

The procedure begins with the thermal simulation performed based on the procedure presented in Sect. 2. After the thermal simulation is completed, the distribution of temperatures is available in the points of the cross-section for every instant of time, respecting the subdivisions adopted in Eq. 4 and Eq. 5. Once the temperature and the constitutive relationship of the FRC at that temperature are known, the equations for the rotational and translational stability of the cross-section can be written as:

where n_s is the quantity of subsections in the cross-section; n_{sc} is the quantity of compressed subsections located within $0.8x$; n_{st} is the quantity of subsections subjected to tensile stresses; T_x is the temperature at the position of the neutral axis; $T_{0.8\times}$ is the temperature at distance $0.2\times$ from the neutral axis; n_{su} is the amount of rebars in the upper region of the section (extrados); n_{sl} is the amount of rebars in the lower region of the section (intrados); A_{su} is the cross-sectional area of steel (unitary) in the upper region; A_{sl} is the cross-sectional area of steel (unitary) in the lower region; H is the initial height of the segment; d_{su}

$$N = B.\left[\sum_{i=1}^{n_{sc}} f_{cd,(T_i)}.\Delta z + f_{cd,(T_{0.8x})}.(0.8x - n_{sc}.\Delta z) - \sum_{i=1}^{n_{st}} f_{Ftud,\left(T_{n_s-n_{si}+i}\right)}.\Delta z - f_{Ftud,(T_x)}.(H - x - n_{st}.\Delta z)\right] + n_{su}.A_{su}.f_{sd,(T_{su},\chi)}.\beta_1 - n_{sl}.A_{sl}.f_{sd,(T_{sl},\chi)}.\beta_2 \tag{18}$$

$$M = B.\left[\begin{array}{r} \sum_{i=1}^{n_{sc}} f_{cd,(T_i)}.\Delta z.\left[\frac{H}{2} - \Delta z.\left(i - \frac{1}{2}\right)\right] + f_{cd,(T_{0.8x})}.(0.8x - n_{sc}.\Delta z).\left[\frac{H}{2} - 0.8x + \frac{0.8x - n_{sc}.\Delta z}{2}\right] \\ + \sum_{i=1}^{n_{st}} f_{Ftud,\left(T_{n_s-n_{si}+i}\right)}.\Delta z.\left[\frac{H}{2} - \left(n_{st} - i + \frac{1}{2}\right).\Delta z\right] + f_{Ftud,(T_x)}.(H - x - n_{st}.\Delta z).\left[\frac{H}{2} - x - \frac{H - x - n_{st}.\Delta z}{2}\right] \end{array}\right] + n_{su}.A_{su}.f_{sd,(T_{su},\chi)}.\left(\frac{H}{2} - d_{su}\right).\beta_1 + n_{sl}.A_{sl}.f_{sd,(T_{sl},\chi)}.\left(\frac{H}{2} - d_{sl}\right).\beta_2 \tag{19}$$

is the concrete cover at the extrados; d_{sl} is the concrete cover at the intrados; and the β_1 and the β_2 variables compute the signal for the contribution of rebars in the rotational and transitional stability equations according to Eq. (20) and Eq. (21), respectively. The latter is required since the failure planes are accounted by inputting a vector of neutral axes x contained between the intrados and extrados of the FRC segment, which is posteriorly necessary for assessing the M–N interaction envelopes.

$$\beta_1 = \begin{cases} \dfrac{d_{su} - x}{|d_{su} - x|} & if\ x \neq d_{su} \\ 0 & if\ x = d_{su} \end{cases} \tag{20}$$

$$\beta_2 = \begin{cases} \dfrac{(x - H + d_{sl})}{|x - H + d_{sl}|} & if\ x \neq (H - d_{sl}) \\ 0 & if\ x = (H - d_{sl}) \end{cases} \tag{21}$$

According to the discussion provided in Sect. 2.2, the spalled layers are removed from the analysis whenever the spalling criteria is reached. The mechanical model computes the spalled layers by setting the respective coefficient of mechanical degradation at those layers to zero (*i.e.* $K_c = K_{Ftu} = K_{sy} = 0$). The adoption of this procedure means the formulations presented in Eq. 18 and Eq. 19 remain the same even when spalling is considered. However, the mechanical contribution of the spalled layers to the overall bearing capacity is null due to being factored by zero in Eqs. 15–17.

3.3 Validation of the model

The validation of the thermal model was conducted by exposing steel fiber reinforced concrete (SFRC) prismatic specimens to a vertical fire simulator, following the same experimental procedure presented by Serafini et al. [30]. The experimental setup and heating regime aimed to reproduce the heating conditions at the intrados of a tunnel lining. Prismatic specimens measuring 150 × 150 × 550 mm were produced containing thermocouples positioned at preset distances of 3, 6, 9, 12, and 15 cm from the surface subjected to fire. The prismatic specimens were positioned in structural masonry wall and exposed to a unifacial heat regime following the HFC (Fig. 4a). The validation of the mechanical model was carried out by testing the fire-exposed prismatic specimens under bending according to EN 14,651 [34], being the region closer to the fire maintained facing downward during the test (Fig. 4b).

Both the experimental and numerical fire-induced temperature distributions are presented in Fig. 5a. These results allow confirming that the errors of the thermal model are below 11% for t = 120 min, independently of the depth in the SFRC specimen. Likewise, it is to be remarked that errors decrease as the exposure time t increases, the maximum error being below 42% (t < 20 min) in all cases. The latter, however, is not significant from the design perspective since the drop of bearing capacity starts to be noticeable for time exposure superior to 15 min, at which the thermal model provides reliable results. Therefore, the thermal model resulted to be capable of

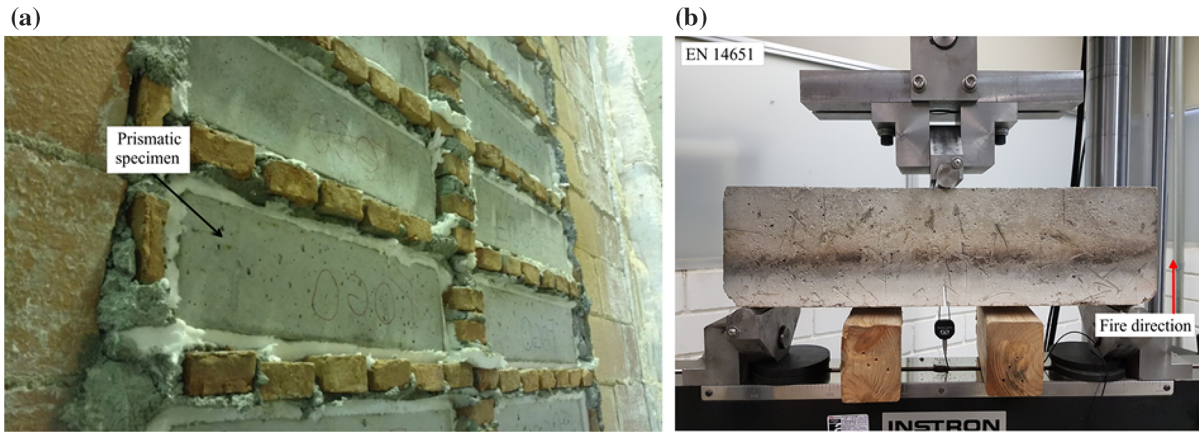

Fig. 4 **a** Prismatic specimens positioned and **b** bending test configuration

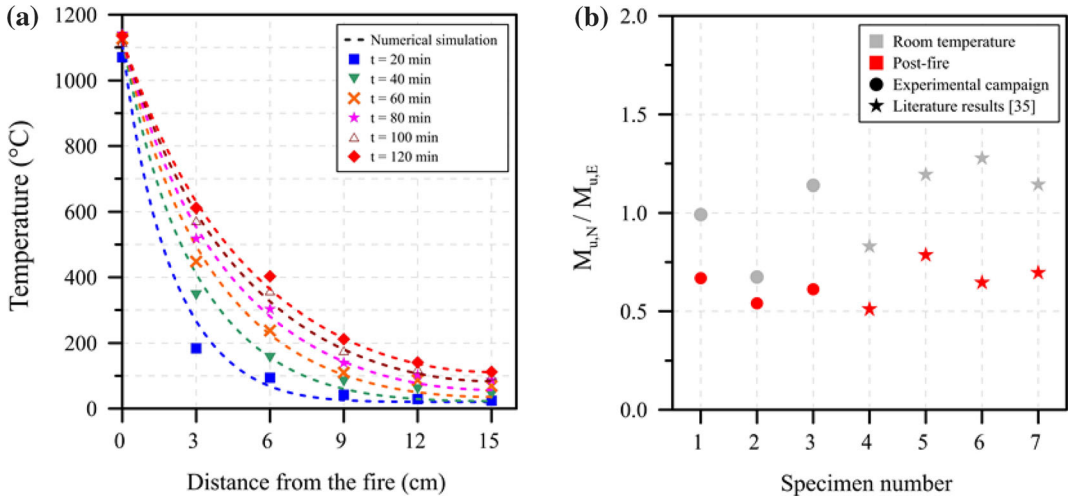

Fig. 5 **a** Fire-induced temperature distribution and **b** $M_{u,N}/M_{u,E}$ considering the experimental and numerical results

predicting the distribution of temperatures within the section, with sufficient accuracy for structural design purposes, especially when considering long-time fire exposures.

For validation purposes, the resisting bending moment at CMOD = 2.5 mm ($M_{u,E}$) was determined based on the load-CMOD curves by imposing equilibrium conditions. The $M_{u,E}$ was then compared to the bearing capacity obtained numerically ($M_{u,N}$) by computing the ratio $M_{u,N}/M_{u,E}$ (Fig. 5b), which provides information on both the model accuracy and the margin of safety respect to the experimental results. Likewise, the results presented by Agra [35] were also been included into the database in order to increase the representativeness of this validation. In this regard, it must be remarked that Agra used the same materials and proportions, while also following the experimental procedure exposed in Serafini et al. [30]. However, Agra tested smaller prismatic specimens of 100 × 100 × 350 mm, which does not affect the results of this validation.

The results presented in Fig. 5b permit to draw the following conclusions regarding the mechanical model validation: (1) the mean $M_{u,N}/M_{u,E}$ for room temperature is 1.04 (CoV = 20.8%), which confirms the capability of the model to predict the bearing capacity of SFRC elements subjected to normal temperature. Moreover, this CoV = 20.8% is aligned with the expected variability of both the post-cracking flexural strength of SFRCs and the accuracy of the constitutive equations and material partial safety factors provided in the *fib* MC-2010 for simulating the post-cracking response of SFRC specimens [36]. And (2), for post-fire conditions, the average $M_{u,N}/M_{u,E}$ is 0.64 (CoV = 14.7%), which denotes that the mechanical model yields to conservative results, with rather low dispersion of the results (taking into account the intrinsic scatter of the SFRC post-cracking mechanical properties [37]). This may be justified by the adoption of constitutive equations that may not precisely represent the thermal-related changes in mechanical properties (*i.e.* distribution of the damage along the cross-section), but are in favor of safety and accepted in the design guidelines [27, 28]. Based on the outcomes of these validations, the prediction capacity and accuracy of both models were found to be satisfactory and sufficient for the purpose of this research.

4 Numerical investigation

In light of the discussions provided in the previous sections, a parametric investigation was conducted aiming to assess the effect of fire in the bearing capacity of the RC and FRC sections. The space–time domain was discretized considering $\Delta z = 2.5$ mm and $\Delta t = 1$ s, which were values employed to validate the thermal model when comparing to the results obtained by Di Carlo et al. [16]. The following scenarios were employed to assess the deterioration of bearing capacity on RC and FRC sections exposed to fire:

(1) A conventional RC with A_s = 792 mm^2 on the upper region and lower region of the section. This value was chosen since it is minimum longitudinal reinforcement ratio for compressed members according to the *fib* MC-10, which aims to ensure the ductility response in case of cracking due to transient loads related to transportation, stacking, and manipulation of the segments. The sensitivity to fire action was evaluated on a RC section with a concrete cover of c = 30 mm (RC30) based on the XC4 exposure class prescribed by the *fib* MC-10 [28], and another RC section with c = 50 mm (RC50).

(2) A FRC 45 3c composite without any steel rebar reinforcement. This solution can be used in those lining stretches along which low-moderate forces are expected and minimum amount of reinforcement is required, in which the conventional rebar reinforcement is replaceable by fibers. Likewise, local reinforcement is required to control splitting and spalling cracks due to the thrust of the jacks during excavation.

(3) A FRC 45 3c composite with the same steel reinforcement described in (1), being identified as RC30-FRC for the hybrid option with c = 30 mm, and RC50-FRC for the one with c = 50 mm. This hybrid reinforcement approach could be of technical interest in those stretches along which the external forces are demanding in magnitude and/or cracking is expected due to the thrust of the TBM, resulting in the need for additional reinforcement to control cracking.

These possible configurations for the cross-section of the tunnel were analyzed in this paper as a function of the temperature-time pattern numerically obtained, based on the fire curve adopted and the axial load ratio applied. Table 1 shows the input parameters adopted for the thermo-mechanical simulations conducted in this study.

4.1 Effect of fire curve and reinforcement type

First, the simulation was conducted considering one mild fire scenario and one severe fire scenario, thus following, respectively, the ISO 834 and the HFC fire curves. These fire curves were employed on the RC, FRC, and RC-FRC solutions. Moreover, the reduction in bearing capacity is presented for two axial loading conditions: (1) considering simple bending to be representative of lining stretches or sections where the axial load is low in magnitude (*i.e.* $N/A_c.f_{cd,25\ ^\circ C} = 0$); (2) considering a 0.20 axial load ratio to be representative stretches placed at medium-large buried sections. Figure 6 illustrates the changes in bearing capacity of the sections exposed to the HFC and the ISO 834 fire curves. At this moment, the analysis is conducted without considering the occurrence of thermal spalling.

For all reinforcement types, the reductions in bearing capacity were lower for the sections affected by the ISO-834 than those affected by the HFC, independently of the magnitude of the axial load. This difference is more pronounced for lower values of t, which is a reasonable considering that the ISO-834 fire curve prescribes lower heating rate and lower maximum temperature values than the HFC. The reduction in FRC 45 3c simple bearing capacity caused by the HFC was 3.5% to 5.5% greater than the reductions caused by the ISO-834, which shown to be a range valid for all values of t. Therefore, the FRC solution showed low sensitivity to the characteristics of the fire curves, which may be attributed to the distributed reinforcement and the reduced contribution of the f_{Ftu} to the sectional bearing capacity [16]. In this sense, the FRC simple bearing capacity reduced by $\sim$ 31% and $\sim$ 35% after t = 120 min of ISO 834 and HFC fire curve, respectively.

The RC30 simple bearing capacity reduced by $\sim$ 73% and $\sim$ 84% when exposed to the respective ISO-834 and HFC fire curves after t = 120 min, whereas the RC50 bearing capacity reduced by $\sim$ 22% and $\sim$ 35%. Therefore, the increase in concrete cover considerably reduced the sensitivity of the RC solution to fire, independently of the fire curve adopted. This decreased fire-sensitivity is associated with the lower temperatures developed in steel and the consequently reduced mechanical deterioration of the rebars, as shown in Fig. 7. A more rapid increase in temperature is verified for rebars located at c = 30 mm than for c = 50 mm, which is also more pronounced when the RC solutions are exposed to HFC than when exposed to the ISO-834 fire curve.

The hybrid solution RC30-FRC showed a simple bearing capacity reduction of $\sim$ 59% and $\sim$ 63% when exposed to the respective ISO-834 and HFC fire

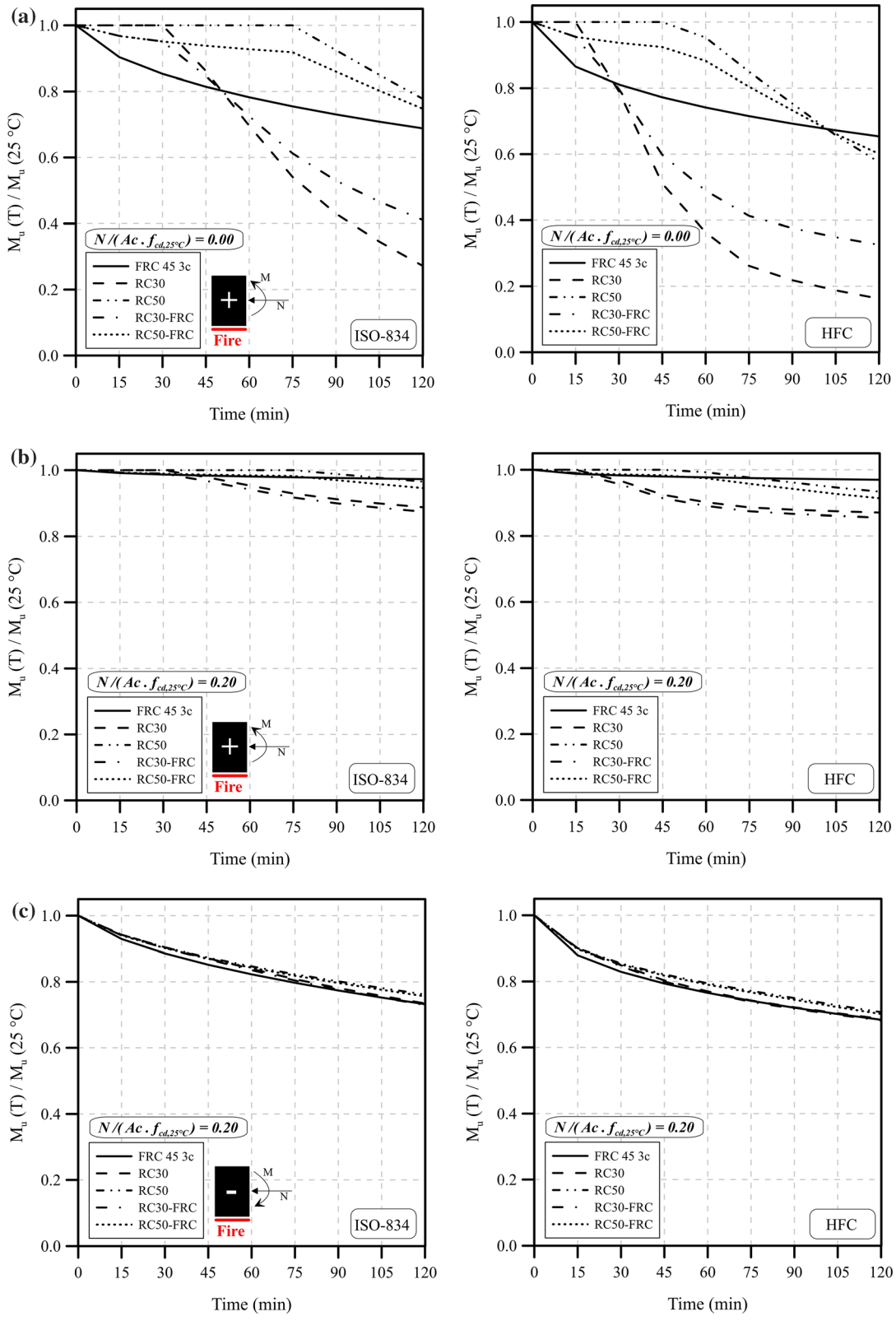
(a)
(b)
(c)
M_u (T) / M_u (25 °C)
Time (min)
$N/(Ac \cdot f_{cd,25°C}) = 0.00$
$N/(Ac \cdot f_{cd,25°C}) = 0.20$
FRC 45 3c
RC30
RC50
RC30-FRC
RC50-FRC
Fire
M
N
ISO-834
HFC

◀**Fig. 6** Changes in bearing capacity of the sections exposed to **(a)** the ISO 834 and **(b)** the HFC fire curves

curves after $t = 120$ min, while the RC50-FRC showed reductions of ~ 25% and ~ 40%. In this sense, it is possible to observe that the RC and hybrid RC-FRC solutions are considerably more sensitive to the different fire curves than the FRC solution, which is justified by the considerable contribution of the localized reinforcement provided by rebars to the bearing capacity. Moreover, lower reductions in simple bearing capacity are noticed for RC50 and RC50-FRC for fire durations lower than ~ 90 min, which can be attributed to the additional protection to rebars given by the increase in concrete cover.

Given the severe nature of the HFC, the analysis henceforth is focused on the results obtained by sections exposed to this particular fire curve. When comparing the RC-FRC and the RC solutions, the RC30-FRC section showed lower reductions than those observed for RC30, especially for $t \geq 30$ min. Contrarily, the reductions in RC50-FRC bearing capacity were greater than those obtained by RC50, especially during the first 90 min of the fire, reaching a comparable reduction for $t = 120$ min. These results show that the addition of fibers to RC sections is beneficial particularly when the reinforcement

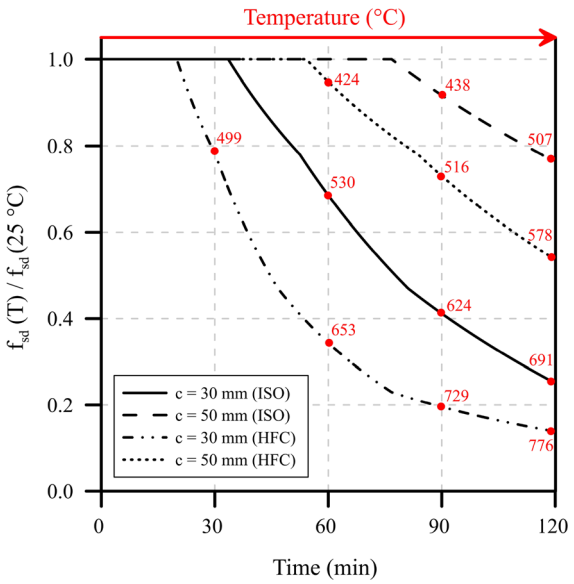

Fig. 7 Distribution of temperatures and the respective reduction in the yield strength of rebars

provided by rebars is considerably reduced during the fire. However, when the rebars remain relatively unaffected by temperature, a slight reduction in bearing capacity is noticed due to the deterioration of the fibrous reinforcement. Therefore, the behavior of RC-FRC sections is highly dependent on the position of rebars and is directly associated with the contribution of fibers to the bearing capacity.

The RC50 and RC50-FRC solutions obtained the lowest reductions in bearing capacity, except for fire durations greater than ~ 90 min, in which FRC yielded lower reductions. Nevertheless, the RC30 solution was the most fire sensitive option among all the reinforcement solutions and fire scenarios evaluated. When the solutions are axially loaded and subjected to sagging bending moments, the reductions in the bearing capacity are considerably mitigated This was evidenced for all reinforcement types and it occurs because a failure mode based on the crushing of the compressive layer that is not affected by fire occurs. Given the fact that fire affects the flexural tensile region of the section, RC30 and RC30-FRC have yielded the greatest reductions in bearing capacity under sagging bending moments with an axial load ratio of 0.2.

The results showed that the reductions in bearing capacity are not dependent on the reinforcement type for axially loaded sections under hogging bending moments. This non-dependance of reinforcement type is justified by the greater reduction in the compressive strength of concrete and the lower influence of the reinforcement type in this regard. Sections under hogging bending moments yielded the greatest reductions in bearing capacity among the axially loaded sections, which denotes that this condition must be verified for the fire safety assessment of tunnels.

Moreover, the results proved that the cross-sectional ductility (represented by the curvature, χ) increases with the fire duration, as shown in Fig. 8. This increase was greater for RC30 and RC30-FRC alternatives, independently of the axial load ratio. Among the RC and RC-FRC solutions, the RC50 and RC50-FRC solution have shown similar ductility increments and obtained the lowest increase in ductility due to the lower effective depth of the reinforcement. For simple bending, the FRC obtained the lowest increase in ductility after $t = 120$ min. When the section is subjected to a 0.20 axial load ratio, the RC solutions and the respective hybrid alternatives

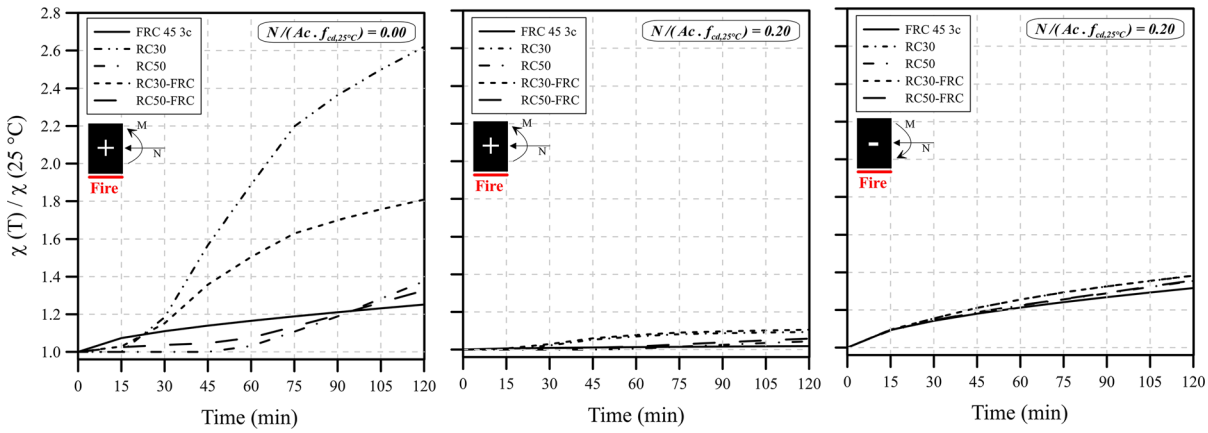

Fig. 8 Effect of fire on the ductility of the reinforcing solutions when affected by HFC

have shown similar ductility patterns and the FRC solution had the lowest increase in ductility, which occurs due to the failure being governed by concrete crushing. The increase in ductility is greater for axially loaded sections exposed to hogging bending moments due to the considerable reductions in compressive strength of the layers closer to the fire.

4.2 Effect of thermal spalling

In light of the bearing capacity reductions presented in Sect. 4.1, the effect of thermal spalling was evaluated considering the HFC since it has proven to be the worst fire scenario evaluated in this study. Experimental results in literature demonstrated the dependance between the onset of thermal spalling and the thermal gradients in normal-strength concrete without microfibers, in which spalling began at $t = 2$ min when exposed to RWS fire curve [31]. In order to ensure a conservative approach, the spalling was considered to begin at $t = 0$ min for simulation purposes.

The reduction in bearing capacity of the sections is evaluated considering two spalling parameters: the spalling rate (R_{sp}) and the percentage of section lost (s_L). These parameters may be determined by measuring the spalling depth as a function of time in experimental campaigns using fire simulators and a concrete representative of the structure [30]. Considering the parametric nature of this study, R_{sp} values of 100 mm/h and 300 mm/h were adopted as moderate and severe spalling rates based on parameters of a normal-strength concrete without microfibers and with different moisture contents [31]. The s_L values of 5%, 10%, and 20% were arbitrarily adopted based on the hypothesis that greater section losses would represent extremely severe cases [15, 20]. In this paper, the spalling rate and section lost values were assumed the same for FRC and RC in order to isolate the effect of reinforcement type on the bearing capacity. However, it is important to remind that the spalling related variables depend also on the reinforcement type – which needs to be taken into account for applications in practice. In this sense, the changes in the height of the section as a function of time and the spalling parameters is presented in Fig. 9.

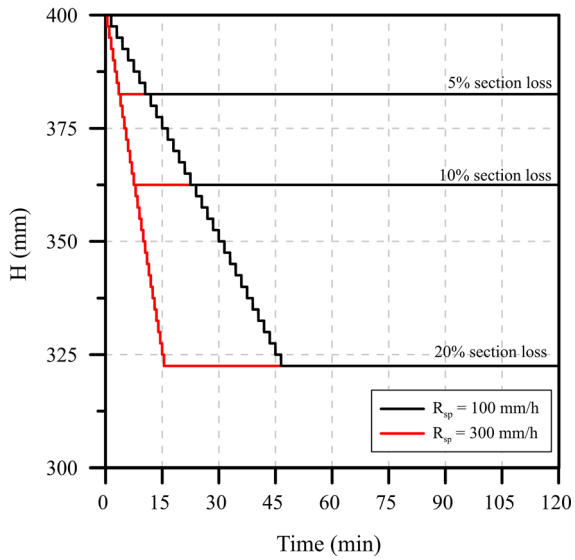

Fig. 9 Change in the height of the section as a function of time and the spalling parameters

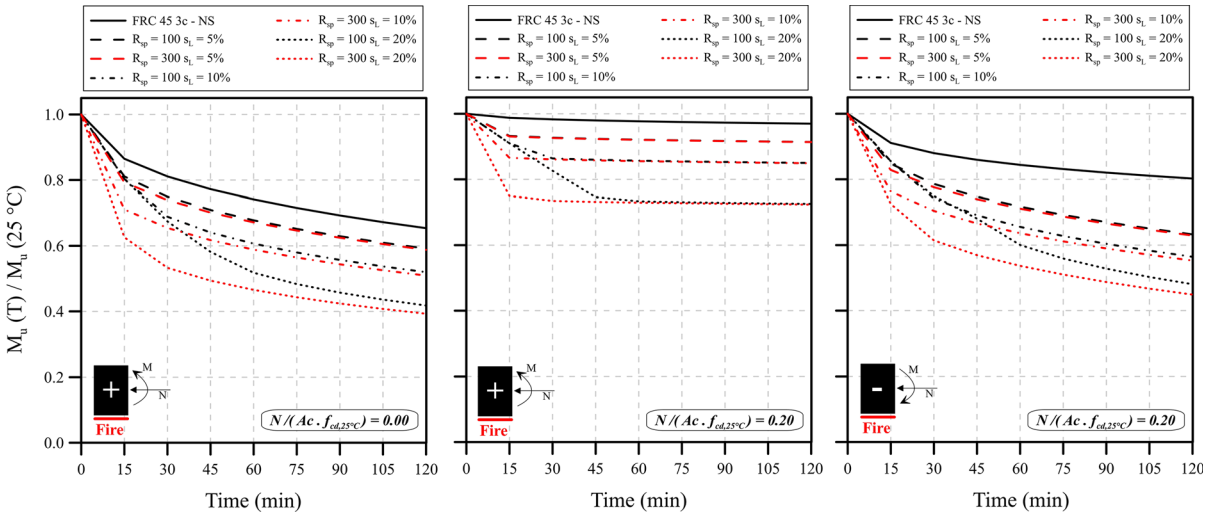

Fig. 10 Reductions in bearing capacity of FRC 45 3c section as a function of R_{sp} and s_L

Considering the aforementioned parameters, the deterioration of the FRC section as a function of R_{sp} and s_L is presented in Fig. 10. The simulations considering the thermal-spalling yielded lower residual bearing capacity than the scenario without the occurrence of thermal spalling – which is recognized by the NS identifier (*e.g.* FRC 45 3c—NS). For a fire duration of t = 120 min, the post-fire bearing capacity seems to be greatly influenced by reductions in s_L and less influenced by the increase in R_{sp}. This can be observed for simple bending, as well for sections with an axial load ratio of 0.20. However, the increase in R_{sp} considerably influences the rate of reduction in the bearing capacity for the initial moments of fire, with exception of s_L = 5%. Regarding the FRC simple bending scenario, reductions of ∼ 40%, ∼ 49%, and ∼ 60% occurred for the respective s_L values of 5%, 10%, and 20% after t = 120 min. For axially loaded sections, the worst reductions were verified for sections under hogging bending moment in which the bearing capacity reduced by ∼ 37%, ∼ 46%, and ∼ 53% for the respective s_L values of 5%, 10%, and 20% after t = 120 min.

Figure 11 illustrates the reductions in bearing capacity of RC30 and RC30-FRC solutions as a function of R_{sp} and s_L. Regarding the RC30 section, the occurrence of thermal spalling reduced the simple bearing capacity by over 90% within the first 30 min of fire, with minimal influence of R_{sp} and s_L. This occurs because the temperature on the rebars increase rapidly given the proximity with the heated surface and the occurrence of thermal spalling, as depicted in Fig. 12. Regarding the RC30-FRC section, the results indicate that the addition of fibers resulted in a solution that is less sensitive to thermal-spalling than the RC30 counterpart. The RC30-FRC simple bearing capacity reduced by ∼ 76%, 82%, and 87% for the respective s_L values of 5%, 10%, and 20% after t = 120 min. Even with this consideration, the bearing capacity of both the RC30 and RC30-FRC sections are drastically reduced when thermal spalling occurs.

Figure 13 illustrates the reductions in bearing capacity of RC50 and RC50-FRC solutions. Considering t = 120 min, the occurrence of thermal spalling reduced the simple bearing capacity of RC50 sections by over 88% independently of the s_L value. However, when s_L = 5% the rate of reduction in bearing capacity is slightly lower than for greater s_L values. For greater s_L values, reductions of over ∼ 80% are registered within the first 30 min of fire. These drastic reductions are a result of the rapid increase in temperature of the rebars due to the reductions in H and the aggravated thermal field induced in the section (see Fig. 12). Although the RC50-FRC solution seems to be slightly less sensitive than RC50, the reductions bearing capacity were greater than 65% after t = 120 min.

Therefore, the occurrence of spalling considerably affects the bearing capacity of FRC, RC, and hybrid RC-FRC sections. The RC30 and RC50 and their respective hybrid options have shown to be very

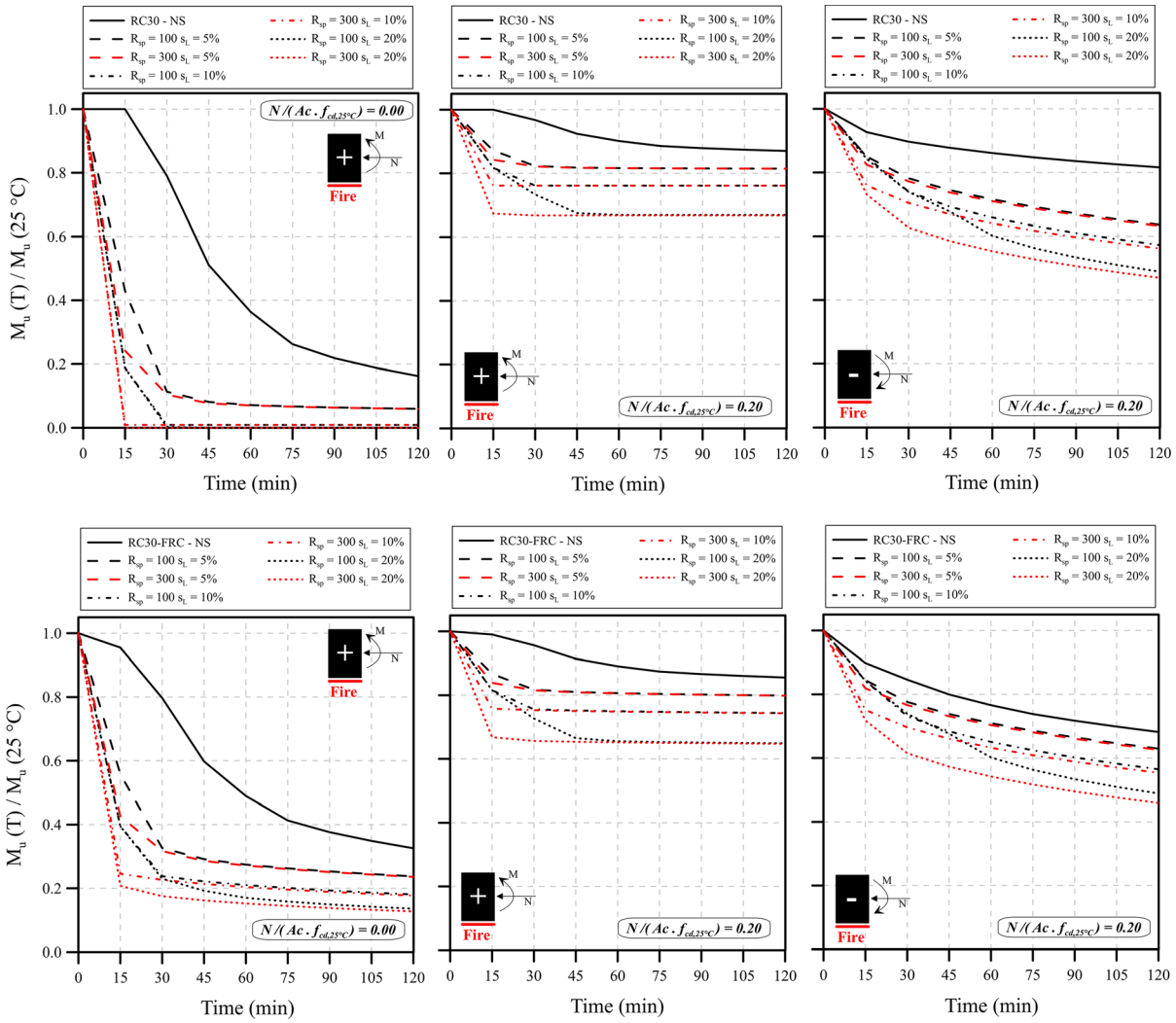

Fig. 11 Reductions in bearing capacity of **(a)** RC30 and **(b)** RC30-FRC solutions as a function of R_{sp} and s_L

sensitive to the occurrence of thermal spalling, since the reductions in H resulted in a more pronounce exposure of the rebars and aggravated thermal field. Therefore, the increase in concrete cover had almost negligible influence in mitigating the reductions in bearing capacity in thermal spalling scenarios. Moreover, the RC-FRC solutions have shown slightly lower bending reductions than the respective RC solution, which indicates that the addition of fibers may mitigate the reductions. Lastly, the FRC solution have shown to be the least sensitive option evaluated, especially for lower s_L values. This occurred because of the contribution of fibers to the sectional bearing capacity and the distributed nature of the fibrous reinforcement.

For axially loaded sections, the sections under hogging bending moments experienced the greatest reductions with and without thermal spalling. The reinforcement type had negligible influence on the reduction values, which may be attributed to the failure mechanism being governed by concrete crushing. Therefore, sections subjected to hogging bending moments yielded the greatest reductions in bearing capacity among the axially loaded sections, which needs to be taken into account for applications in practice.

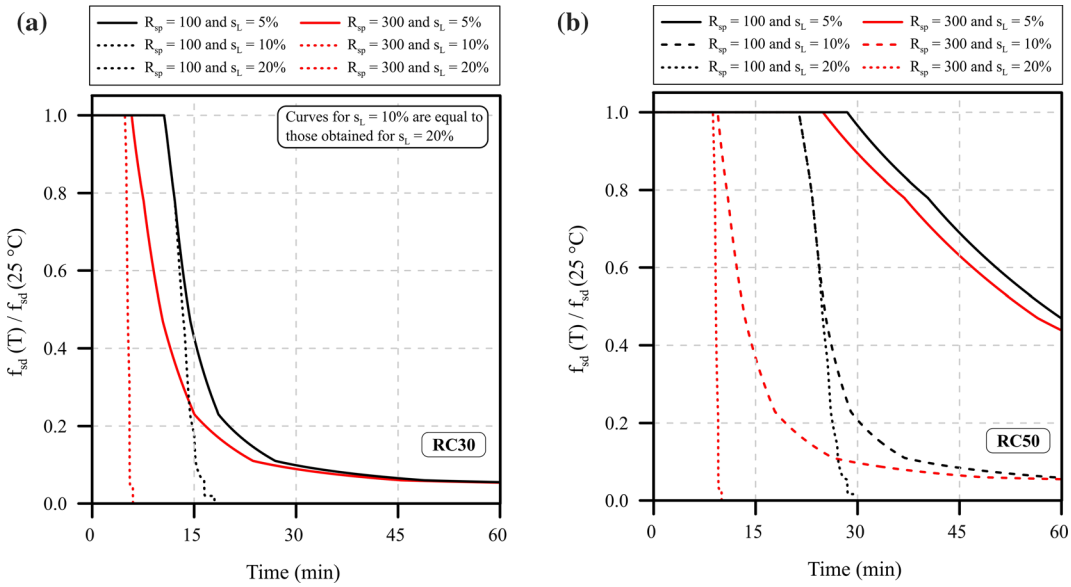

Fig. 12 Effect of R_{sp} and s_L on the tensile strength of rebars in **(a)** RC30 and **(b)** RC50 sections

5 Conclusions

In this research paper, a numerical model for the evaluation of the bearing capacity of cross-sections subjected to fire loads and the thermal spalling effects was implemented, taking as basis the model proposed by Di Carlo et al. [16]. Posteriorly, the model was used to perform a parametric analysis for which reinforced concrete (RC), fiber reinforced concrete (FRC), and the hybrid solution (RC-FRC) were analyzed involving different axial load levels, fire curves, concrete cover and thermal spalling parameters. In this context, based on the results obtained, the following conclusions could be drawn:

(1) Sections exposed to the hydrocarbon fire curve suffered greater bearing capacity reductions than those exposed to the ISO 834 fire curve, independently of the magnitude of axial load. When spalling is inexistent, both FRC and RC50-FRC solutions proved to be less sensitive to fire in comparison with the conventional RC30 solution.

(2) The cross-sectional ductility, represented by the curvature (χ), increases with the fire duration. The increase was greater for RC30 and RC30-FRC alternatives, independently of the axial load ratio. For simple bending, the RC50 and RC50-FRC have shown similar ductility increments, while the FRC obtained the lowest increase in ductility at t = 120 min. When the section is subjected to a 0.20 axial load ratio, the RC solutions and the respective hybrid alternatives have shown similar ductility patterns and the FRC solution had the lowest increase in ductility.

(3) The increase in spalling rate (R_{sp}) influences the rate of reduction in the bearing capacity at the early stage of the fire, while the increase in section lost ratio (s_L) influence the bearing capacity at intermediate-final stages of the fire. This influence was evidenced for all reinforcing strategies and axial load ratios evaluated in this parametric study.

(4) The RC sections analyzed experienced a drastic bearing capacity reduction with the occurrence of thermal spalling, being greater than $\sim$ 90% for RC30 and $\sim$ 80% for RC50. The increase in concrete cover had a minor role in mitigating the reductions of bearing capacity. Although a considerable deterioration is observed, the FRC solution yielded the lower reductions in bearing capacity among all the reinforcing solutions tested.

(5) The reductions in bearing capacity are lower for cross-section subjected to axial load and sagging bending moments. This was evidenced for

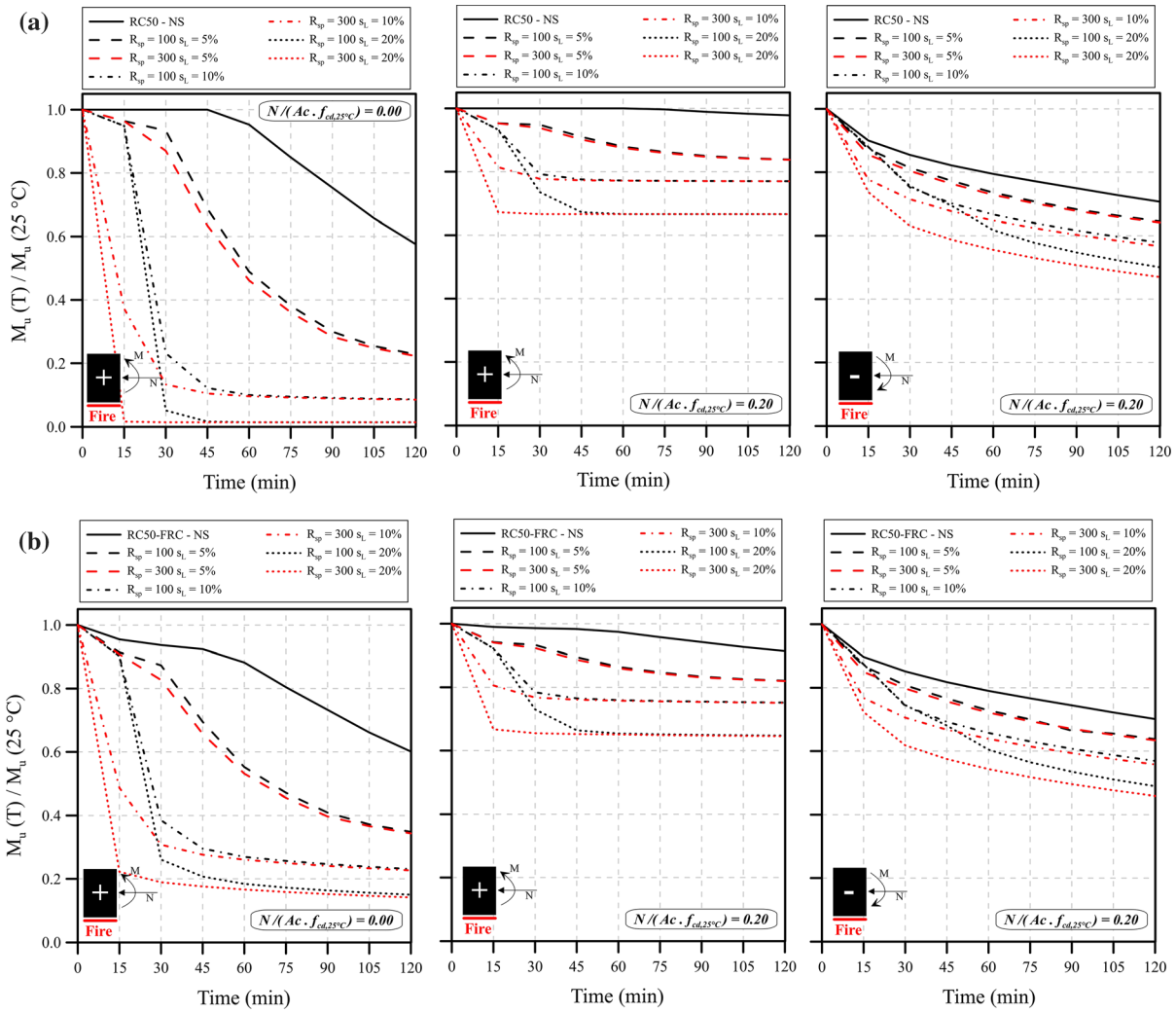

Fig. 13 Reductions in bearing capacity of **(a)** RC50 and **(b)** RC50-FRC solutions as a function of R_{sp} and s_L

all the reinforcement solutions evaluated in this study, with and without thermal spalling. This occurs because the mode of failure changes to crushing of the most compressive concrete layer, which is further from the heating surface and, thus, less affected by fire. However, sections subjected to hogging bending moments yielded the greatest reductions in bearing capacity among the axially loaded sections. This denotes that this is a critical condition that must be verified for the fire safety assessment of tunnels, especially for deeply buried sections.

Therefore, the results show that the thermal–mechanical model and the spalling subroutine implemented in this study may be employed to determine the bearing capacity of RC, FRC, and hybrid RC-FRC solutions. At this end, the results represent a valuable reference for standards and guidelines worldwide, as well as for the engineering community given that the procedure serves as a tool for the design and rehabilitation of tunnel structures affected by fire.

Funding This work was funded by the Institute for Technological Research (IPT) and its foundation (FIPT) through the New Talents Program [grant #N.01/2017 (Ramoel Serafini)] and partially funded the Conselho Nacional de Desenvolvimento Científico e Tecnológico (CNPq) [Grant # 305055/2019–4 (Antonio Domingues de Figueiredo)].

Availability of data and material The data that support the findings of this study are available on request from the corresponding author.

Declarations

Conflict of Interest The authors declare that they have no conflict of interest.

Code availability The code is available upon request made directly to the corresponding author.

References

1. de la Fuente A, Pujadas P, Blanco A, Aguado A (2012) Experiences in Barcelona with the use of fibres in segmental linings. Tunn Undergr Sp Technol. https://doi.org/10.1016/j.tust.2011.07.001
2. Caratelli A, Meda A, Rinaldi Z, Romualdi P (2011) Structural behaviour of precast tunnel segments in fiber reinforced concrete. Tunn Undergr Sp Technol 26:284–291. https://doi.org/10.1016/j.tust.2010.10.003
3. de la Fuente A, Blanco A, Armengou J, Aguado A (2017) Sustainability based-approach to determine the concrete type and reinforcement configuration of TBM tunnels linings. case study: extension line to Barcelona airport T1. Tunn Undergr Sp Technol 61:179–188. https://doi.org/10.1016/j.tust.2016.10.008
4. Liao L, de la Fuente A, Cavalaro S, Aguado A (2016) Design procedure and experimental study on fibre reinforced concrete segmental rings for vertical shafts. Mater Des 92:590–601. https://doi.org/10.1016/j.matdes.2015.12.061
5. Granju J-L, Ullah Balouch S (2005) Corrosion of steel fibre reinforced concrete from the cracks. Cem Concr Res 35:572–577. https://doi.org/10.1016/j.cemconres.2004.06.032
6. Maevski IY (2011) Design Fires in Road Tunnels. National Academies Press, Washington, D.C.
7. Zheng WZ, Li HY, Wang Y, Xie HY (2011) Tensile properties of steel fiber-reinforced reactive powder concrete after high temperature. Adv Mater Res 413:270–276
8. Tai Y-S, Pan H-H, Kung Y-N (2011) Mechanical properties of steel fiber reinforced reactive powder concrete following exposure to high temperature reaching 800°C. Nucl Eng Des 241:2416–2424. https://doi.org/10.1016/j.nucengdes.2011.04.008
9. Poon CS, Shui ZH, Lam L (2004) Compressive behavior of fiber reinforced high-performance concrete subjected to elevated temperatures. Cem Concr Res 34:2215–2222. https://doi.org/10.1016/j.cemconres.2004.02.011
10. Serafini R, Santos FP, Agra RR et al (2018) Effect of specimen shape on the compressive parameters of steel fiber reinforced concrete after temperature exposure. J Urban Technol Sustain. 1:10–20. https://doi.org/10.47842/juts.v1i1.7
11. Sukontasukkul P, Pomchiengpin W, Songpiriyakij S (2010) Post-crack (or post-peak) flexural response and toughness of fiber reinforced concrete after exposure to high temperature. Constr Build Mater 24:1967–1974. https://doi.org/10.1016/j.conbuildmat.2010.04.003
12. Serafini R, Agra RR, Salvador RP et al (2021) Double edge wedge splitting test to characterize the design postcracking parameters of fiber-reinforced concrete subjected to high temperatures. J Mater Civ Eng 33:04021069. https://doi.org/10.1061/(ASCE)MT.1943-5533.0003701
13. Rambo DAS, Blanco A, de Figueiredo AD et al (2018) Study of temperature effect on macro-synthetic fiber reinforced concretes by means of Barcelona tests: an approach focused on tunnels assessment. Constr Build Mater 158:443–453. https://doi.org/10.1016/j.conbuildmat.2017.10.046
14. Agra RR, Serafini R, de Figueiredo AD (2021) Effect of high temperature on the mechanical properties of concrete reinforced with different fiber contents. Constr Build Mater 301:124242. https://doi.org/10.1016/j.conbuildmat.2021.124242
15. Yan Z, Zhu H, Ju JW (2013) Behavior of reinforced concrete and steel fiber reinforced concrete shield TBM tunnel linings exposed to high temperatures. Constr Build Mater 38:610–618. https://doi.org/10.1016/j.conbuildmat.2012.09.019
16. Di Carlo F, Meda A, Rinaldi Z (2018) Evaluation of the bearing capacity of fiber reinforced concrete sections under fire exposure. Mater Struct 51:154. https://doi.org/10.1617/s11527-018-1280-2
17. Carpio JM, Serafini R, Rambo D, et al (2019) Assessment of the bearing capacity reduction of FRC elements subjected to fire. In: Proceedings of the fib Symposium 2019: Concrete - Innovations in Materials, Design and Structures. Kraków, Poland. 1378–1386
18. Fu Y, Li L (2011) Study on mechanism of thermal spalling in concrete exposed to elevated temperatures. Mater Struct 44:361–376. https://doi.org/10.1617/s11527-010-9632-6
19. Yasuda F, Ono K, Otsuka T (2004) Fire protection for TBM shield tunnel lining. Tunn Undergr Sp Technol 19:317. https://doi.org/10.1016/j.tust.2004.01.018
20. Yan Z, Zhu H, Woody JuJ, Ding W (2012) Full-scale fire tests of RC metro shield TBM tunnel linings. Constr Build Mater 36:484–494. https://doi.org/10.1016/j.conbuildmat.2012.06.006
21. Zhang Y, Ju JW, Zhu H, Yan Z (2020) A novel multi-scale model for predicting the thermal damage of hybrid fiber-reinforced concrete. Int J Damage Mech 29:19–44. https://doi.org/10.1177/1056789519831554
22. Bosnjak J (2014) Explosive spalling and permeability of high performance concrete under fire: numerical and experimental investigations. University of Stuttgart
23. Periskic G (2009) Development of a 3D thermo-hygro-mechanical model for concrete under fire and application to fastenings loaded in tension. University of Stuttgart
24. Ozbolt J, Periskic G, Reinhardt H-W, Eligehausen R (2008) Numerical analysis of spalling of concrete cover at high temperature. Comput Concr 5:279–293. https://doi.org/10.12989/cac.2008.5.4.279
25. International Tunnelling and Underground Space Association (2016) ITAtech Report n 7 - Design guidance for precast fibre reinforced concrete segments

26. Fédération Internationale du Béton (2008) Bulletin 46 - Fire design of concrete structures - structural behaviour and assessment. Switzerland
27. Fédération Internationale du Béton (2017) Bulletin 83 - Precast Tunnel Segments in Fibre-Reinforced Concrete. Switzerland
28. Federation Internationale du Beton (2013) Model Code for Concrete Structures 2010. Ernst & Sohn, Germany, p 434
29. Crespo MD, Molins C, Marí AR (2013) Effect of variations in thermal-curing cycle on the cracking risk of precast segmental tunnel lining. Constr Build Mater 49:201–213. https://doi.org/10.1016/j.conbuildmat.2013.07.078
30. Serafini R, Dantas SRA, Salvador RP et al (2019) Influence of fire on temperature gradient and physical-mechanical properties of macro-synthetic fiber reinforced concrete for tunnel linings. Constr Build Mater 214:254–268. https://doi.org/10.1016/j.conbuildmat.2019.04.133
31. Kusterle W, Lindbauer W, Hampejs G et al (2004) Technical Report 544: Fire resistance of fibre-reinforced, reinforced and prestressed concrete. Bundesministerium für Verkehr, Innovation und Technologie, Vienna (**[in German]**)
32. BS EN 1992–1–2 (2004) Eurocode 2 Design of concrete structures - Part 1–2: General rules-Structural fire design. Des Concr Struct - Part 1–2 Gen rules-Structural fire Des
33. CNR-DT 204 (2007) Guide for the Design and Construction of Fibre-Reinforced Concrete Structures. Ital Natl Res Counc (CNR), Rome, Italy. https://doi.org/10.14359/10516
34. EN 14651 (2007) Test method for metallic fibred concrete — Measuring the flexural tensile strength (limit of proportionality (LOP), residual). United Kingdom
35. Agra RR (2020) Influence of temperature on the behavior of concrete with diferent fiber content (In Portuguese). Universidade de São Paulo
36. Cugat V, Cavalaro SHP, Bairán JM, de la Fuente A (2020) Safety format for the flexural design of tunnel fibre reinforced concrete precast segmental linings. Tunn Undergr Sp Technol 103:103500. https://doi.org/10.1016/j.tust.2020.103500
37. Cavalaro SHP, Aguado A (2015) Intrinsic scatter of FRC: an alternative philosophy to estimate characteristic values. Mater Struct 48:3537–3555. https://doi.org/10.1617/s11527-014-0420-6